Supporting Information

Bionic intelligent soft actuators: high-strength gradient intelligent hydrogels with diversified controllable deformations and movements

Qian Zhao[a], *Yanjiao Chang*[a], *Zhenglei Yu*[a], *Yunhong Liang*∗[a], Lei Ren∗[b] Luquan Ren[a]

Description of Supplementary Files

Fig. S1. The macroscopic morphology of (a) NFC0, (b) NFC1, (c) NFC2 and (d) NFC3 gradient structure intelligent hydrogels.

Fig. S2. Microstructure of gradient intelligent hydrogels with different NFC contents before entirety infiltration of GO. (a-1)-(a-4) microstructure of four layers in NFC0, (b-1)-(b-4) microstructure of bottom, middle and top parts of NFC1, (c-1)-(c-4) microstructure of bottom, middle and top parts of NFC2 and (d-1)-(d-4) microstructure of bottom, middle and top parts of NFC3.

Fig. S3. Typical FT-IR spectra of gradient intelligent hydrogels with different NFC contents. (a) NFC0, (b) NFC1, (c) NFC2 and (d) NFC3.

Fig. S4. DSC curves of gradient intelligent hydrogels with different NFC contents. (a) NFC0, (b) NFC1, (c) NFC2 and (d) NFC3.

Fig. S5. The distribution characteristics of Young's modulus of gradient intelligent hydrogels with different NFC contents. (a) NFC0, (b) NFC1, (c) NFC2 and (d) NFC3.

Fig. S6. (a) density and (b) moisture content and volume expansion ratio of gradient

[a]*The Key Laboratory of Bionic Engineering, Ministry of Education, Jilin University, Changchun 130025, China.* E-mail: liangyunhong@jlu.edu.cn
[b]*School of Mechanical, Aerospace and Civil Engineering, University of Manchester, Manchester, M139PL.* E-mail: lei.ren@manchester.ac.uk

NFC reinforced gradient intelligent hydrogels exhibited unbroken structure. Compared with NFC0, colour of hydrogels became deep with the increase of NFC content. Moreover, increasing NFC content decreased the thickness and enhanced compactness, respectively. Fig. S1 indicated that addition of NFC played an important role in the variation and mechanical strength of hydrogels.

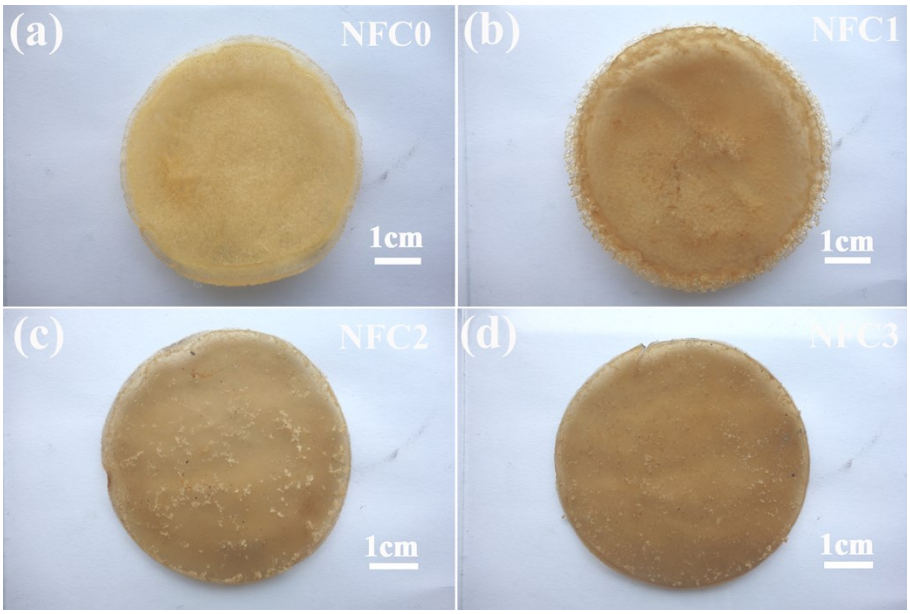

Fig. S1. The macroscopic morphology of (a) NFC0, (b) NFC1, (c) NFC2 and (d) NFC3 gradient structure intelligent hydrogels

Based on micropore size variation, NFC0 gradient intelligent hydrogel can be divided into four layers, as shown in Fig. S2 (a-1)-(a-4). The addition of NFC changed the gradient structure. NFC1 gradient intelligent hydrogel exhibited relatively small size on bottom. The low convex structure existed on micropore surfaces, as shown in Fig. S2 (b-1)-(b-4). NFC2 gradient intelligent hydrogel showed unconspicuous gradient structure. The convex structure on micropore surfaces can be observed clearly in Fig. S2 (c-1)-(c-4). When the NFC content reached 3 mg/mL, thickness of hydrogel decreased further, as shown in Fig. S2 (d-1)-(d-4). The number

of convex structures were also increased.

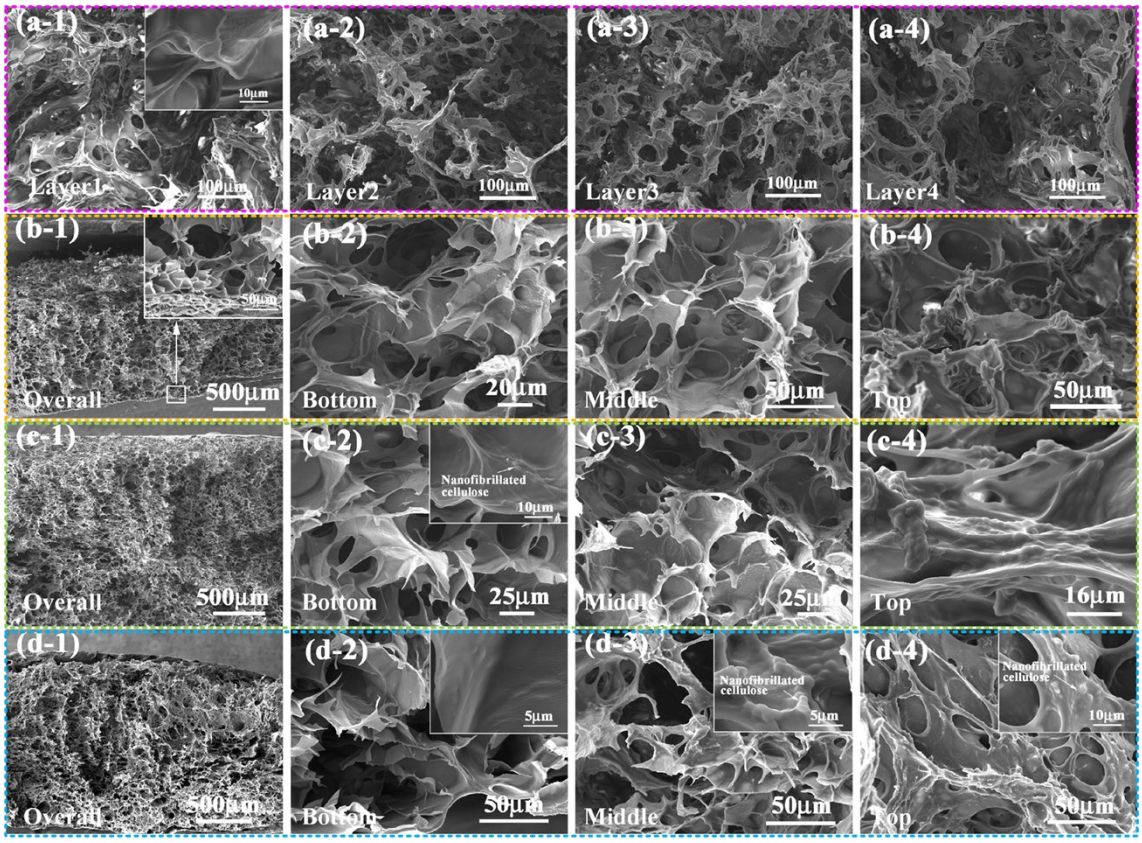

Fig. S2. Microstructure characteristics of gradient intelligent hydrogels with different nanofibrillated cellulose contents before entirety infiltration of GO. (a-1)-(a-4) microstructure of four layers in NFC0, (b-1)-(b-4) microstructure of bottom, middle and top parts of NFC1, (c-1)-(c-4) microstructure of bottom, middle and top parts of NFC2 and (d-1)-(d-4) microstructure of bottom, middle and top parts of NFC3.

As show in Fig. S3 (a), (b), (c) and (d). The broad band between 3200 and 3600 cm^{-1} was the N-H stretching vibration peaks. The band at 1652 cm^{-1} was assigned to the C=O stretching vibration peak. The band at 1546 cm^{-1} was attributed to N-H bending vibration peak. The bands at 1376 cm^{-1} and 1456 cm^{-1} were the absorption peaks of $–CH(CH_3)_2$. The addition and variation of NFC induced the excursion of peak at 1652 cm^{-1}.

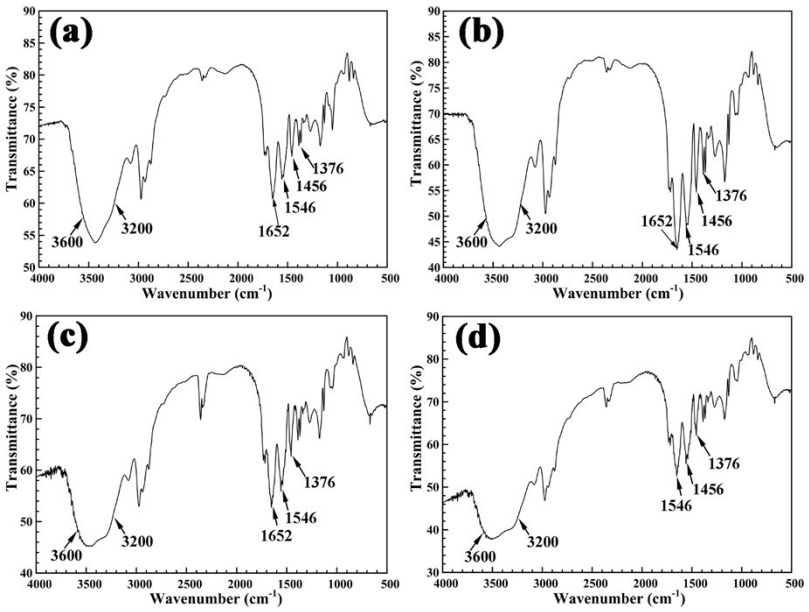

Fig. S3 Typical FT-IR spectra of gradient intelligent hydrogels with different NFC contents. (a) NFC0, (b) NFC1, (c) NFC2 and (d) NFC3.

The volume phase transition temperature (VPPT) of NFC intelligent hydrogel was in the range of 31.9 °C to 33.2 °C, as shown in Fig. S4. Compared with NFC0, addition of NFC changed the VPPT and maintained the temperature response behaviour, which was similar to FT-IR results. Namely, the reinforcement of NFC maintained intelligent property of hydrogels, proving the feasibility of monomer, crosslinking agent and reinforcement in hydrogel material systems.

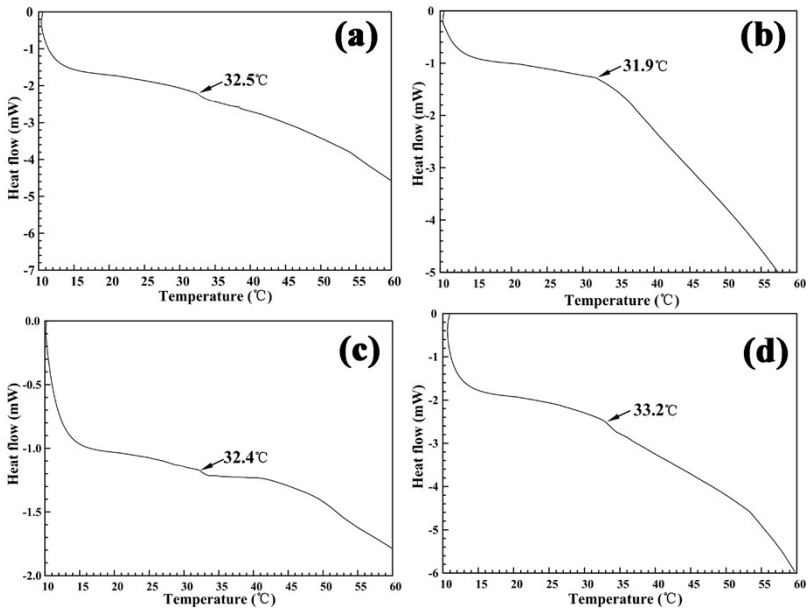

Fig. S4. DSC curves of gradient intelligent hydrogels with different NFC contents. (a) NFC0, (b) NFC1, (c) NFC2 and (d) NFC3.

Based on the Young's modulus range (0.9 KPa-2.7 KPa), NFC0 hydrogel in Fig. S5 (a) can be divided into four layers, which was similar to the result of Fig. 1 and Fig. S2. As shown in Fig. S5 (b), the maximum Young's modulus value of NFC1 hydrogel was 9.9 KPa, which was higher than that of NFC0 hydrogel. Moreover, the thickness of NFC1 was lower than that of NFC0. The weaken gradient structure was also similar to the microstructure analysis result. When the NFC content reached 2 mg/mL, Young's modulus range of NFC2 was 10.9 KPa-11.5 KPa, as shown in Fig. S5 (c). With the increase of NFC content, thickness of NFC2 was decreased further. When the NFC content increased to 3 mg/mL, Young's modulus range of NFC3 was 10.0 KPa-10.7 KPa, as shown in Fig. S5 (d).

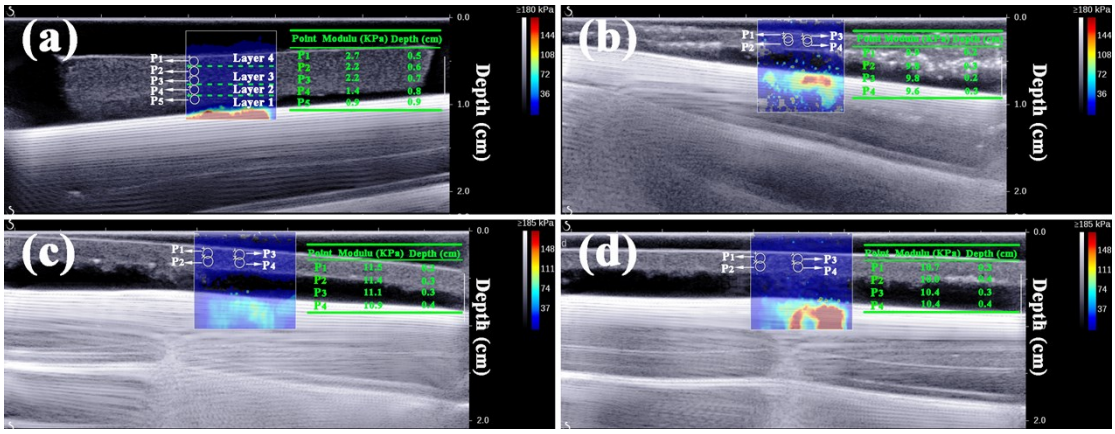

Fig. S5. The distribution characteristics of Young's modulus of gradient intelligent hydrogels with different NFC contents. (a) NFC0, (b) NFC1, (c) NFC2 and (d) NFC3.

Then density (ρ), moisture content (η) and volume expansion ratio (δ) were calculated via the following equations.

$$\rho = \frac{M_d}{V_d} \quad \cdots\cdots(1)$$

$$\eta = \frac{M_e - M_d}{M_e} \quad \cdots\cdots(2)$$

$$\delta = \frac{V_e - V_d}{V_e} \quad \cdots\cdots(3)$$

Where M_d and M_e represented the freeze drying weight and full swollen weight of hydrogels, respectively. V_e and V_d represented the freeze drying volume and full swollen volume of hydrogels, respectively.

As shown in Fig. S6, the densities of NFC0, NFC1, NFC2 and NFC3 intelligent hydrogels were 0.0315 g/cm^3, 0.04835 g/cm^3, 0.0698 g/cm^3 and 0.0764 g/cm^3, respectively. The moisture contents were 0.970, 0.942, 0.939 and 0.934, respectively. The volume expansion ratios were 0.6757, 0.2777, 0.2059 and 0.1288, respectively. Increasing NFC content led to the enhancement of crosslinking density of hydrogels,

which increased the density and decreased the thickness, moisture content and volume expansion ratio, respectively.

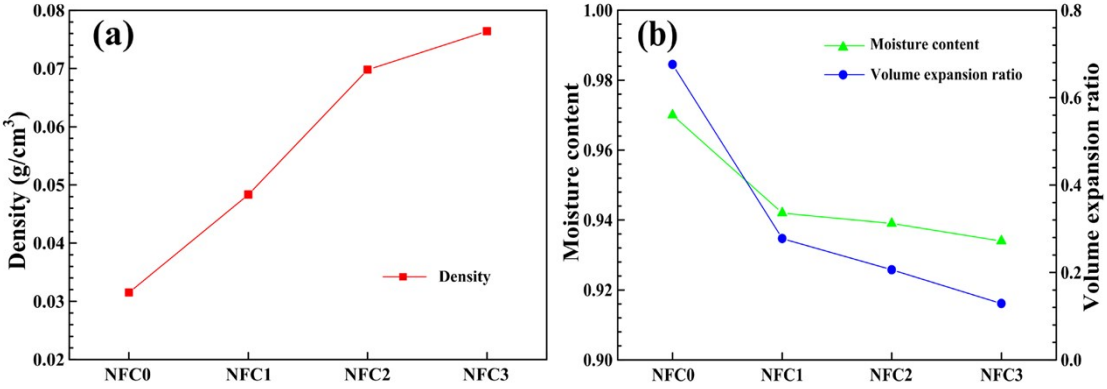

Fig. S6. (a) density and (b) moisture content and volume expansion ratio of gradient intelligent hydrogels with different NFC contents.

The swelling ratio (SR) and deswelling ratio (WR) were calculated as follows:

$$SR = \frac{W_t - W_d}{W_t} \quad \text{.....(4)}$$

$$WR = \frac{100(W_t - W_d)}{W_s - W_d} \quad \text{.....(5)}$$

where W_t (g) represented the weight of the hydrogels at the corresponding time, W_d (g) represented the weight of the dry hydrogels, and W_s (g) represented the weight of the full swollen hydrogels in pure water at 25 °C.

Swelling and deswelling behaviour of intelligent hydrogels was influenced by the variation of NFC content. With the increase of NFC content, the time of hydrogels reached full swollen state was decreased gradually, as shown in Fig. S7 (a). The deswelling ratios in 20 s of hydrogels were increased with the increase of NFC content, as shown in Fig. S7 (b). Combined the swelling and deswelling time, the NFC reinforced intelligent hydrogels owned high intelligent response rate.

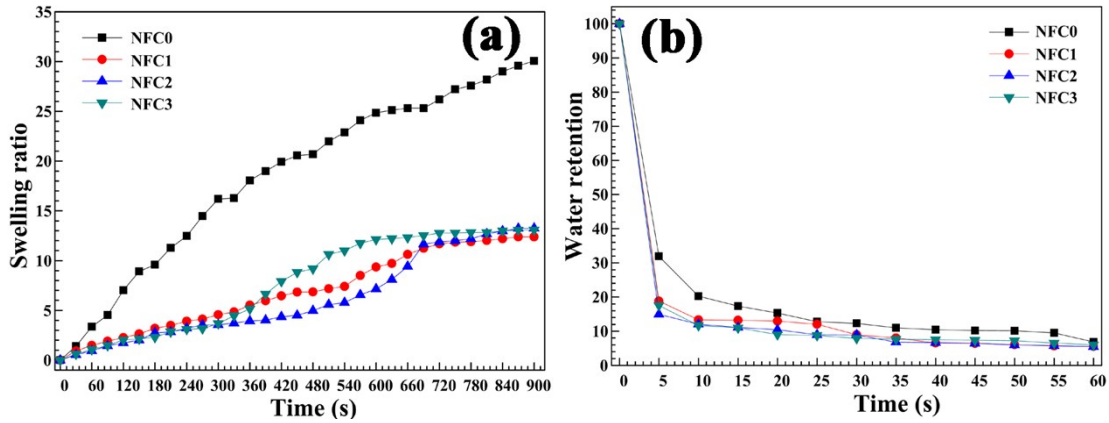

Fig. S7. (a) swelling and (b) deswelling ratio of gradient intelligent hydrogels with different NFC contents.

Fig. S8 (a-1)-(a-6) shows the bionic drosera deformation process of NFC2 intelligent hydrogel, which used 11 s to reach the curled pattern. Compared with NFC0 and NFC1 intelligent hydrogels, NFC2 owned the lowed curling degree. As shown in Fig. S8 (b-1)-(b-6), NFC3 intelligent hydrogel used 11 s to reached curled state. But, the final curling degree of NFC3 was higher than that of NFC2.

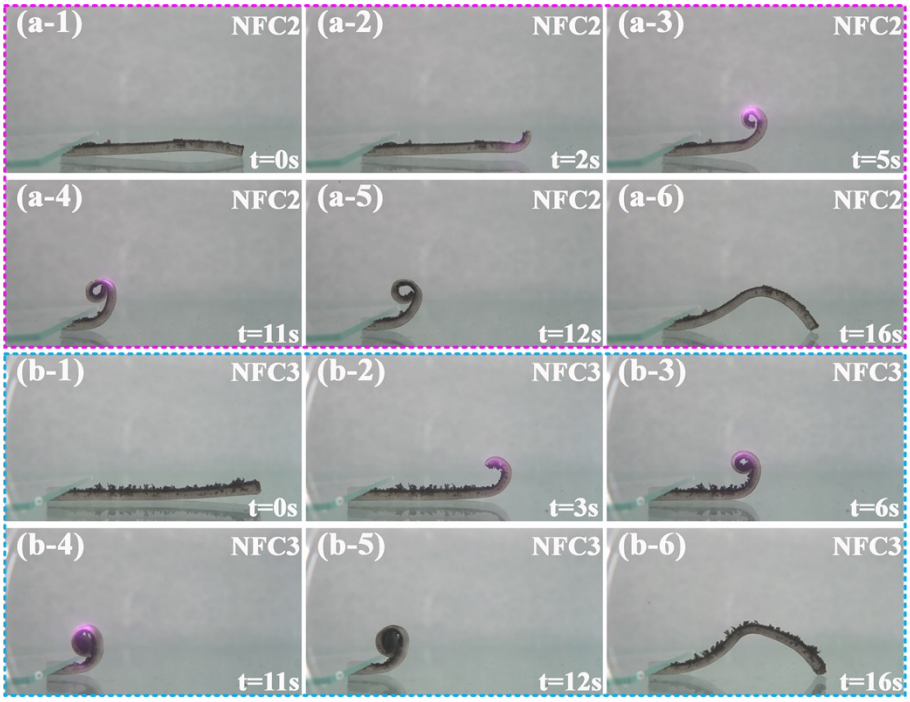

Fig. S8. The bionic drosera deformation processes of (a-1)-(a-6) NFC2 and (b-1)-(b-6) NFC3 gradient intelligent hydrogels.

Combined with the self-driven deformations and movements, the mechanical analysis can be used for analyzing self-driven mechanisms of bending, curling, switching and obstacle avoidance movement. Based on the effect of NFC content on material and mechanical characteristics of gradient intelligent hydrogels, the bending and folding deformation theory was built to influence of different thickness and swelling properties on deformation efficiency. In order to be convenient for mechanical analysis, assumed conditions were constructed in Fig. S9. The simplified model of NFC reinforced gradient intelligent hydrogels can be divided into two layers. Every layer was homogeneous material and owned specific thickness.

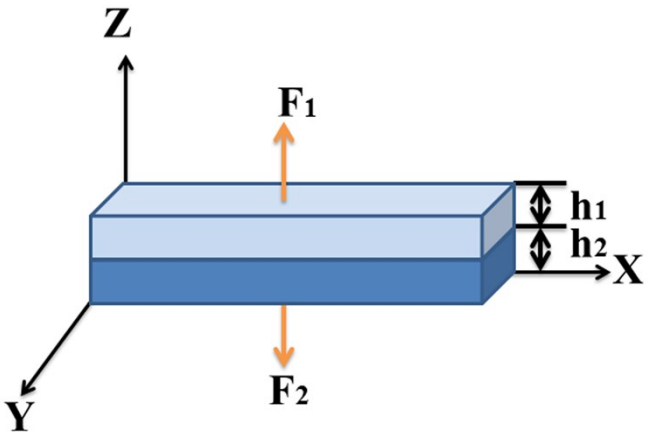

Fig. S9. The simplified model of NFC reinforced gradient intelligent hydrogels.

The simplified model was in equilibrium state without external forces, which can be described as equations (6) and (7).

$$F_1 = -F_2 = F \quad \text{.....(6)}$$

$$\frac{Fh}{2} = M_1 + M_2 \quad \text{.....(7)}$$

Where F_1 and F_2 were axial forces of every layer. M_1 and M_2 represented the corresponding bending moments. Strength values of every layer were $\frac{E_1 h_1^3}{12}$ and $\frac{E_2 h_2^3}{12}$,

respectively. Therefore, equation (7) can be rewrote as follows:

$$\frac{Fh}{2} = \Delta\kappa\left(\frac{E_1 h_1^3}{12} + \frac{E_2 h_2^3}{12}\right) \quad \text{.....(8)}$$

$\Delta\kappa$ represented the variation of slope of intelligent hydrogel. h_1 and h_2 were thickness of every layer in Fig. S9. $h=h_1+h_2$. E_1 and E_2 were Young's modulus of every layer. Based on the displacement equality of bilayer structure in deformation process, equation (9) can be described as follows:

$$\alpha_1\Delta\phi + \frac{F_1}{E_1 h_1} + \Delta\kappa\frac{h_1}{2} = \alpha_2\Delta\phi + \frac{F_2}{E_2 h_2} + \Delta\kappa\frac{h_2}{2} \quad \text{.....(9)}$$

Where $\Delta\phi$ was relative humidity. α_1 and α_2 were expansion factors of two layers. The curvature equation can be obtained by organizing (8) and (9).

$$\Delta\kappa = \frac{\alpha\Delta\phi f(m,n)}{h} \quad \text{.....(10)}$$

$\alpha = \alpha_1 - \alpha_2 \neq 0$. $f(m,n)$ was assumed the function of thickness ratio (m) and Young's modulus ratio (n), as shown in equation (11).

$$f(m,n) = \frac{6(1+m)^2}{3(1+m)^2 + (1+mn)(m^2 + 1/mn)} \quad \text{.....(11)}$$

$m = \frac{h_1}{h_2}$. $n = \frac{E_1}{E_2}$. Combined with the real thickness ratio scale and Young's modulus ratio scale, numerical ranges of m and n in $f(m,n)$ were stetted. $0.2 \le m \le 2$. $0.4 \le n \le 3.1$. The function curve of $f(m,n)$ was built by the range of m and n, as shown in Fig. S10.

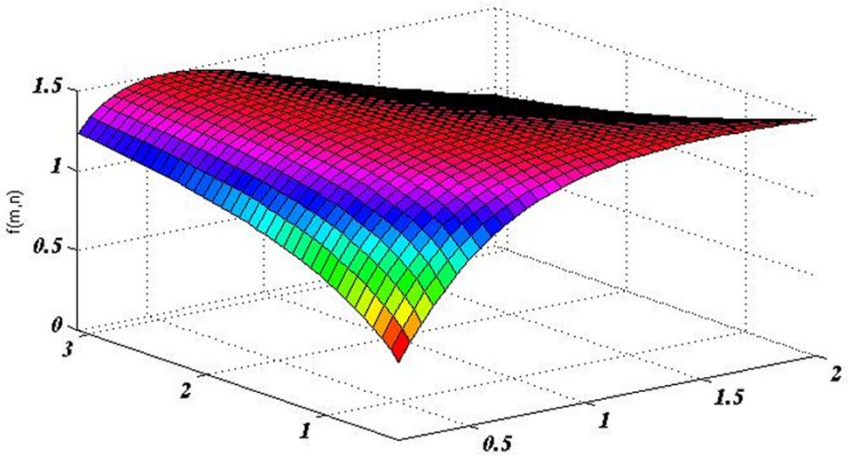

Fig. S10. The function curve of the simplified model of gradient intelligent hydrogels.

When the material property and stimulation condition were specific values, $C = \alpha\Delta\phi/h$. C was constant coefficient. The curvature function (10) can be listed as follows.

$$\Delta\kappa = Cf(m,n) \quad \text{.....(12)}$$

Equation (12) constructed the congruent relationship of curvature, thickness ratio and Young's modulus ratio. Variation of NFC content affected the Young's modulus. Curvature values affected bending degree of NFC reinforced intelligent hydrogels, which influenced the bending deformation characteristics. In deformation of "Polymer", every letter was obtained by curvature variation, exhibiting the bending deformation. With the increase of irradiation time of NIR, the curvature values of intelligent hydrogels were enhanced and ended at an upper limit value of curvature, which realized the specific letter shape in Fig. 10.

Without considering the other forces, equation (13) can be listed as follows on the base of newton's second law.

$$F = (m_1 + m_2)a \quad \text{.....(13)}$$

m_1 and m_2 were weights of every layer in Fig. S9. a was the accelerated velocity

of simplified model. Combined with equation (13) and (8), velocity *v* and displacement y can be described as equation (15) and (16).

$$a = \frac{\Delta\kappa}{h(m_1 + m_2)}\left(\frac{E_1 h_1^3}{6} + \frac{E_2 h_2^3}{6}\right) \quad \text{.....(14)}$$

$$v = \frac{\Delta\kappa t}{h(m_1 + m_2)}\left(\frac{E_1 h_1^3}{6} + \frac{E_2 h_2^3}{6}\right) \quad \text{.....(15)}$$

$$y = \frac{\Delta\kappa t^2}{2h(m_1 + m_2)}\left(\frac{E_1 h_1^3}{6} + \frac{E_2 h_2^3}{6}\right) \quad \text{.....(16)}$$

The corresponding deformation displacement can be calculated by the known material properties of intelligent hydrogels. Equation (16) constructed the relationship between displacement and curvature. Curvature variations induced by NIR were corresponded to displacement values. On the base of intermittent NIR irradiation, curvature values and bending displacement of the NFC hydrogels exhibited repeating and cyclic changing process.

Under the continuous variation of curvature values, the displacement value of NFC reinforced gradient intelligent hydrogels were changed continuously. Curling deformation resulted from bending deformation. Continuous displacement variation led to continuous displacement curves. The NFC0 bionic drosera sample was divided into 10 parts. Every part was treated as a mass point. By superposing the displacement of every mass point, the deformation curves of bionic drosera were obtained, as shown in Fig. S8. Displacement values of actual sample were measured. The mass, thickness and Young's modulus of intelligent hydrogels with different NFC contents were fixed properties. Fig. S11 exhibited characteristics of Equation (16), proving the effectiveness of self-driven explanation of curling deformation by curvature.

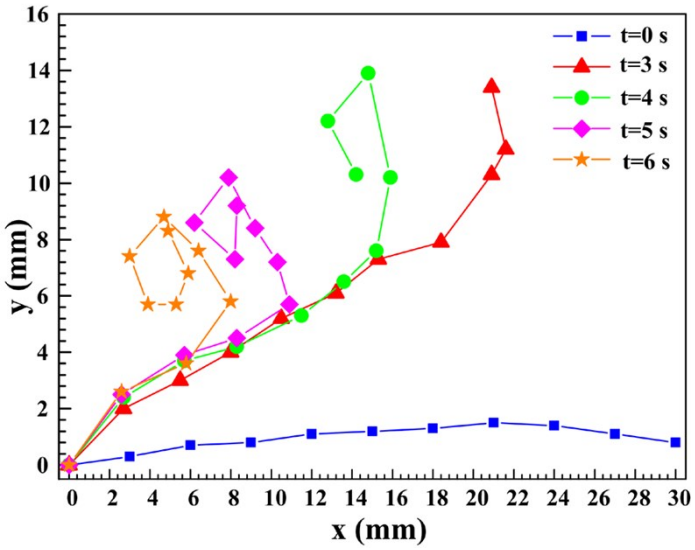

Fig. S11. The curve prediction of bionic drosera deformation.

In order to investigate the self-driven mechanism of the switching, "forward" and "turn" movement, Foppl-von Karman elastic theory was used to analyse the plane bending phenomenon. The NFC reinforced gradient intelligent hydrogels were assumed to elastic sheet without stress, as shown in Fig. S12. The infinitesimal of elastic sheet was selected to conduct mechanical analysis.

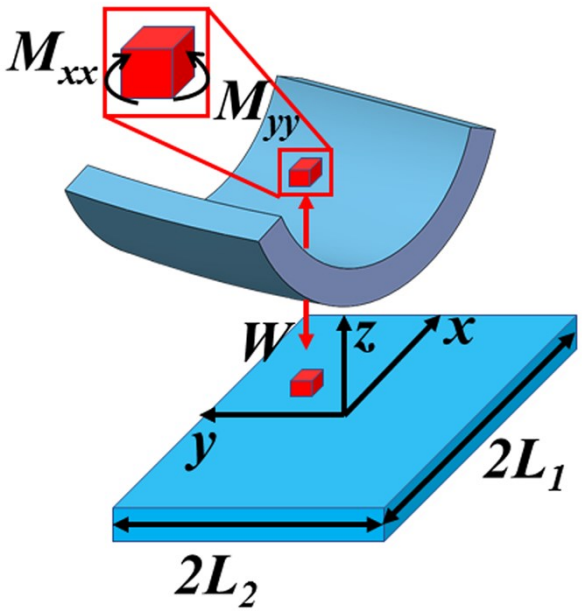

Fig. S12. The schematic diagram of elastic sheet before and after deformation.

The curvature value of elastic sheet in bending process was assumed positive. According to Foppl-von Karman elastic theory, Equation (17) was described as follows:

$$\frac{1}{E}\nabla^4\Phi = -\frac{1}{2}[S,S] - \nabla_\kappa^2 S - \nabla^2(\alpha P) \quad \text{.....(17)}$$

Φ represented the airy stress function. E was Young's modulus of intelligent hydrogels. $\nabla^4\Phi = \partial^4(\Phi)/\partial x^4 + \partial^4(\Phi)/\partial y^4 + 2\partial^4(\Phi)/\partial x^2\partial y^2$. $\partial^4(\Phi)/\partial x^2\partial y^2 = 0$. $E = (E_1h_1 + E_2h_2)/h$. The expansion factor was $\alpha = (\alpha_1h_1 + \alpha_2h_2)/h$. The laplace operator was $\nabla_\kappa^2 = \kappa_y\,\partial^2/\partial x^2 + \kappa_x\,\partial^2/\partial y^2$. κ_y and κ_x were curvature of NFC reinforced intelligent hydrogels on *y* axis and *x* axis, respectively. The displacement inner product was $[S,S] = 2(\partial^2 S/\partial x^2\,\partial^2 S/\partial y^2 - (\partial^2 S/\partial x\partial y)^2)$. The excitation factor *P* was assumed linearly independent to displacement. Therefore, $\nabla^2(\alpha P) = \partial^2(\alpha P)/\partial x^2 + \partial^2(\alpha P)/\partial y^2 = 0$. The displacement of elastic sheet *S* can be described as follows.

$$S = -\frac{1}{2}\kappa_x x^2 - \frac{1}{2}\kappa_y y^2 \quad \text{.....(18)}$$

Equation (17) can be organized as follows.

$$\partial^4(\Phi)/\partial x^4 + \partial^4(\Phi)/\partial y^4 = E\kappa_x\kappa_y \quad \text{.....(19)}$$

After twice integral of *x* and *y* in Equation (19), the accelerated velocity function was Equation (20).

$$\begin{cases} \partial^2(\Phi)/\partial x^2 = E\kappa_x\kappa_y(x^2/2 - L_1^2/6) \\ \partial^2(\Phi)/\partial y^2 = E\kappa_x\kappa_y(y^2/2 - L_2^2/6) \end{cases} \quad \text{.....(20)}$$

On the base of torque balance principle, Equation (21) can be listed as follows.

$$\begin{cases} \int_{-L_1}^{L_1} \sum M dx = \int_{-L_1}^{L_1} \sum M_{yy} + (h\partial^2(\Phi)\Big/\partial x^2)(-\kappa_x x^2/2)dx = 0 \\ \int_{-L_2}^{L_2} \sum M dy = \int_{-L_2}^{L_2} \sum M_{xx} + (h\partial^2(\Phi)\Big/\partial y^2)(-\kappa_y y^2/2)dx = 0 \end{cases} \quad \ldots(21)$$

The bending moment of elastic sheet can be described by Equation (22)

$$\begin{cases} M_{xx} = D\left(\dfrac{\partial^2 S}{\partial x^2} + \mu\dfrac{\partial^2 S}{\partial y^2}\right) - \dfrac{Eh^2\alpha\theta}{12(1-\mu)} \\ M_{yy} = D\left(\dfrac{\partial^2 S}{\partial y^2} + \mu\dfrac{\partial^2 S}{\partial x^2}\right) - \dfrac{Eh^2\alpha\theta}{12(1-\mu)} \end{cases} \quad \ldots\ldots\ldots\ldots\ldots\ldots\ldots\ldots(22)$$

Where μ was Poisson's ratio. *D* was constant. After adding Equation (22) into Equation (21), κ_y and κ_x can be listed as follows.

$$\begin{cases} \dfrac{2}{45}\kappa_x\kappa_y^2 L_1^4 + \dfrac{h^2(\kappa_x + \mu\kappa_y)}{6(1-\mu^2)} + \dfrac{\alpha P(h-2z^*)}{1-\mu} = 0 \\ \dfrac{2}{45}\kappa_x^2\kappa_y L_2^4 + \dfrac{h^2(\kappa_y + \mu\kappa_x)}{6(1-\mu^2)} + \dfrac{\alpha P(h-2z^*)}{1-\mu} = 0 \end{cases} \quad \ldots\ldots\ldots\ldots\ldots(23)$$

The middle plane of material was defined as $z^* = \int zEdz \Big/ \int Edz$. $L_2 \approx L_1$ was assumed.

By organizing Equation (23), Equation (24) can be listed as follows.

$$(\kappa_x - \kappa_y)(4\kappa_x\kappa_y L_1^4(1+\mu) - 15h^2) = 0 \quad \ldots\ldots\ldots\ldots\ldots\ldots\ldots\ldots\ldots(24)$$

By using Rayleigh-Ritz method, $\kappa_x = \kappa_y$ or $\kappa_x\kappa_y = [(1+\mu)L_1^4 - 15h^2]/4$ can satisfy the energy conservation. When $\kappa_x = \kappa_y$, longitudinal curvature was equal to transverse curvature. The elastic sheet bent to its origin of coordinates. When $\kappa_x\kappa_y = [(1+\mu)L_1^4 - 15h^2]/4$, longitudinal curvature was inversely proportional to transverse curvature, as shown in Fig. S13. Under the condition of specific material properties, longitudinal curvature and transverse curvature can be calculated by Equation (23).

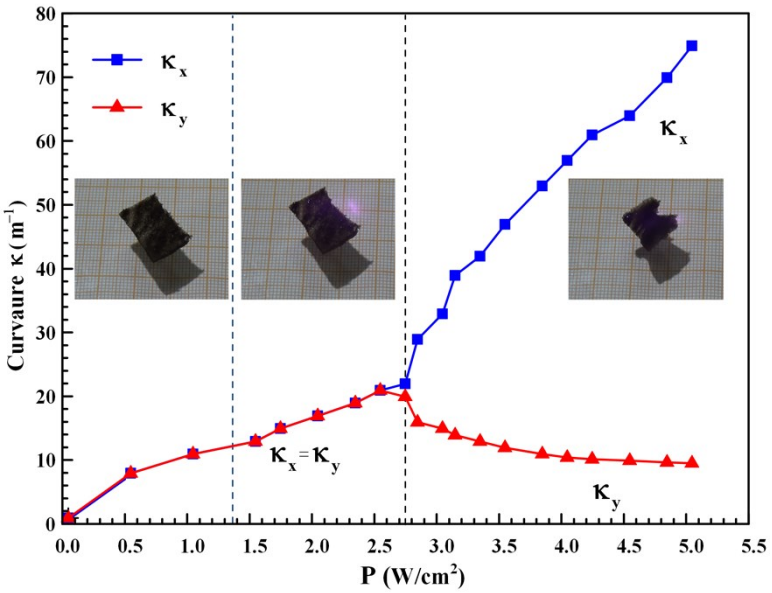

Fig. S13. The change relation curves of elastic sheet and incentive intensity.

Combined with Equations (21), (22) and (23), incentive intensity (NIR power intensity) value affected κ_x and κ_y directly. With the increase of incentive intensity, the relationship between κ_x and κ_y changed from equality to inverse. Different NIR power densities affected torque values of NFC reinforced gradient intelligent hydrogels on *x* axis and *y* axis, respectively, which realized 90 °circulatory switching and homodromous circulatory switching.

The variation of NIR irradiation patterns affected the incentive intensity and irradiation time which intelligent hydrogels obtained, inducing indeterminacy factors in the "forward" and "turn" movement process. Therefore, two movement trails in Fig. 7 existed obvious misalignment. The elastic sheet structure of NFC2 intelligent hydrogel with obstacle avoidance movement owned low thickness, which can realize bending deformation easily. The buckling deformation patterns of NFC reinforced gradient intelligent hydrogels were influenced by geometry characteristic and material anisotropy. The deformation curvature including material properties, irradiation time

and NIR power density directly affected the driven force of NFC2 intelligent hydrogels in obstacle avoidance movement process. Therefore, the movement direction of NFC2 intelligent hydrogel was affected by material distribution homogeneity and irradiation position stability, which realized the functional properties in Fig. 7. Under the assumed conditions of homogeneous material, same irradiation time and position, NFC reinforced gradient intelligent hydrogels can realize ideal movement condition along with fixed direction and patterns. But, attributed to the manual control of NIR, the irradiation distance and position were not constancy, which exhibited movement patterns in Movie S7 and S8.